Available online at www.sciencedirect.com
ScienceDirect
Journal of Sound and Vibration 299 (2007) 504–519
JOURNAL OF SOUND AND VIBRATION
!?tbklnk = "else" > www.elsevier.com/locate/jsvi

A frequency domain numerical method for airfoil broadband self-noise prediction

Qidou Zhou[a], Phillip Joseph[b,*]

[a]*Ship Science Department, 717 Jie Fang Road, Wuhan 430033, PR China*
[b]*Institute of Sound and Vibration Research, University of Southampton, Highfield, Southampton, SO17 1BJ, UK*

Received 1 April 2005; received in revised form 9 June 2006; accepted 14 June 2006
Available online 10 October 2006

Abstract

This paper describes a numerical approach, based in the frequency domain, for predicting the broadband self-noise radiation due to an airfoil situated in a smooth mean flow. Noise is generated by the interaction between the boundary layer turbulence on the airfoil surface and the airfoil trailing edge. Thin airfoil theory is used to deduce the unsteady blade loading. In this paper, the important difference with much of the previous work dealing with trailing edge noise is that the integration of the surface sources for computation of the radiated sound field is evaluated on the actual airfoil surface rather than in the mean-chord plane. The assumption of flat plate geometry in the calculation of radiation is therefore avoided. Moreover, the solution is valid in both near and far fields and reduces to the analytic solution due to Amiet when the airfoil collapses to a flat plate with large span, and the measurement point is taken to the far field.

Predictions of the airfoil broadband self-noise radiation presented here are shown to be in reasonable agreement with the predictions obtained using the Brooks approach, which are based on a comprehensive database of experimental data. Also investigated in this paper is the effect on the broadband noise prediction of relaxing the 'frozen-gust' assumption, whereby the turbulence at each frequency comprises a continuous spectrum of streamwise wavenumber components. It is shown that making the frozen gust assumption yields an under-prediction of the noise spectrum by approximately 2dB compared with that obtained when this assumption is relaxed, with the largest occurring at high frequencies.

This paper concludes with a comparison of the broadband noise directivity for a flat-plat, a NACA 0012 and a NACA 0024 airfoil at non-zero angle of attack. Differences of up to 20 dB are predicted, with the largest difference occurring at a radiation angle of zero degrees relative to the airfoil mean centre line.

1. Introduction

Airfoil self-noise is the noise produced by an airfoil situated in a smooth, non-turbulent in-flow. It is generated by the interaction between the turbulence produced in the boundary layer on the blade surface and the airfoil trailing edge. This paper presents a numerical approach, based in the frequency domain, for predicting the self-noise radiation from airfoils of realistic geometry situated in a uniform mean flow.

*Corresponding author. Tel.: +44 23 80592172; fax: +44 23 80593190.
E-mail address: pfj@isvr.soton.ac.uk (P. Joseph).

0022-460X/$ - see front matter © 2006 Elsevier Ltd. All rights reserved.
doi:10.1016/j.jsv.2006.06.061

In this paper we adopt the general approach proposed by Amiet [1], whereby the airfoil surface pressure spectrum in the absence of the trailing edge is used as the input quantity for making self-noise predictions. Once this surface pressure is known, it then remains to establish the relationship between the radiated sound and the surface pressure induced by the turbulence upstream of the trailing edge. Chase [2] was one of the first to employ this general philosophy for making trailing edge noise predictions. However, the Kutta condition was not satisfied by this solution and mean flow effect were not included. Chandiramani [3] subsequently obtained a solution for the acoustic field in which only the scattered pressure satisfies the trailing edge Kutta condition. This solution was later used by Chase [4] in a model of airfoil trailing edge noise. A more complete formulation of airfoil self-noise radiation, which includes mean-flow effects, and which correctly satisfies the Kutta condition, was developed by Amiet [1]. Although his solution is only valid for two-dimensional flat plate airfoil geometries, it is a closed-form result that clearly establishes the relationship between the pressure jump across the flat plate due to the scattered pressure and the pressure incident upon the trailing edge from one side of the airfoil. Amiet's solution is restricted to normal-incidence, harmonic plane wave pressure components. Howe [5] has extended this solution to include harmonic plane wave pressure waves impinging at oblique angles to the trailing edge, but does not include mean flow effects. Recently Roger and Moreau [17] have extended Amiet solution [1,18] to include the leading edge correction for oblique gusts. In order to obtain an analytic solution for the far field radiated pressure, Amiet made several assumptions: (1) the observation point is at the geometric far field; (2) the airfoil is a flat plate; and (3) the airfoil span is large compared to acoustic wavelength. In this paper, the general solution for the scattered surface pressure due to an oblique gust with mean flow effects, will be used, which is obtained following the method proposed by Amiet in a subsequent paper [6]. This relationship, together with an assumed form for the boundary layer pressure spectrum, is used in a numerical procedure aimed at computing the aerodynamic source strengths from which the broadband self-noise radiation is then predicted. The method presented in the paper circumvents the simplifying assumptions made by Amiet and can take account of the effects of airfoil thickness and angle of attack, and is also valid in both the far field and near field.

2. Coordinate systems

The analysis presented here of the radiated acoustic field from an airfoil is formulated in a Cartesian coordinate system $\mathbf{y} = (y_1, y_2, y_3)$, which moves with constant velocity U, as shown in Fig. 1. It will be shown to be useful to express the airfoil surface pressure in the curvilinear coordinate system, $\boldsymbol{\eta} = (\eta_s, \eta_t)$, attached to the airfoil. Here $\boldsymbol{\eta}$ are used as an auxiliary variable to specify the two-dimensional airfoil surface. Here, $\eta_s = \eta_s(\mathbf{y})$ is the streamwise coordinate of the pressure or suction side, originating at the trailing edge, and $\eta_t = \eta_t(\mathbf{y})$ is the spanwise coordinate originating at the mid-span along the suction-side or pressure-side trailing edges. Correspondingly, we define k_s and k_t as the turbulence wavenumber in the η_s- and η_t-direction, respectively. For a flat plate airfoil, $(\eta_s, \eta_t) = (y_1, y_2)$ and $(k_s, k_t) = (k_1, k_2)$.

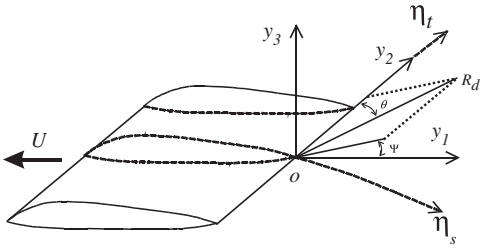

Fig. 1. Curvilinear coordinates $\boldsymbol{\eta} = (\eta_s, \eta_t)$, spherical coordinate system (R_d, Ψ, θ), and rectangular coordinate systems $\mathbf{x}(x_1, x_2, x_3)$, $\mathbf{y}(y_1, y_2, y_3)$.

3. Green function solution

Our starting point for the prediction of airfoil broadband noise is the Green function solution of the forced wave equation derived from the acoustic analogy. This is the fundamental equation governing the generation of aerodynamic sound in the presence of solid boundaries, whose Green function solution takes the form (for example, Goldstein [7], Eq. (4.10))

$$p(\mathbf{x},t)=\int_{-T}^{T}\iiint_{v(\tau)}\frac{\partial^2 G}{\partial y_i\partial y_j}T'_{ij}(\mathbf{y},\tau)d^3\boldsymbol{y}\,\mathrm{d}\tau+\int_{-T}^{T}\iint_{S(\tau)}\frac{\partial G}{\partial y_i}f_i\mathrm{d}S(\mathbf{y})\,\mathrm{d}\tau+\int_{-T}^{T}\iint_{S(\tau)}\rho_0 V'_n\frac{D_0 G}{D\tau}\,\mathrm{d}S(\boldsymbol{y})\,\mathrm{d}\tau, \tag{1}$$

where f_i is the ith component of the force per unit area exerted by the boundaries on the fluid, T'_{ij} is Lighthill's stress tensor for isentropic flow in a region $v(\tau)$, V'_n is the normal velocity of blade surface $S(\tau)$, the superscript primes on T'_{ij} and V'_n indicate the quantities are measured in the earth-fixed reference frame, t is the time associated with the arrival of sound wave at the observation point $\mathbf{x}$, τ is the time associated with emission of sound wave at the source point $\mathbf{y}$ and T is some large but finite interval of time. In Eq. (1), $G=G(\mathbf{x},t;\mathbf{y},\tau)$ is the Green function solution for the wave equation relating to a medium with uniform mean flow. In an unbounded medium, G is given by [8]

$$G(\mathbf{x},t;\mathbf{y},\tau)=\frac{1}{4\pi R}\delta\left[\tau+\frac{1}{\beta^2 c_0}(R+M(y_1-x_1))-t\right], \tag{2}$$

where $\beta^2=1-M^2$, $M=U/c_0$ is the Mach number of the mean flow, δ is the Dirac delta function, and R is the mean-flow corrected distance,

$$R=\sqrt{(y_1-x_1)^2+\beta^2(y_2-x_2)^2+\beta^2(y_3-x_3)^2}. \tag{3}$$

Note that the velocity U, which appears in the Green function G, is the airfoil velocity rather than local incoming velocity U_0 due to potential flow effects. For an infinite flat-plate airfoil, both U and U_0 are airfoil velocities with the subscript '0' being used to indicate a quantity related to the source on the airfoil surface, for example, the Mach number M_0, β_0, and the frequency ω_0 (note that source frequency and observer frequency differ in the case of a rotor). In general, U_0 is used to indicate the local mean flow velocity at the interface of the boundary layer. In this case U_0 equals U plus the local potential velocity due to the effects of airfoil thickness and boundary layer displacement thickness. The effect of this local mean flow on the airfoil surface pressure is taken into account through the position-dependent function of Eq. (16), and eventually through the incident surface pressure spectrum S_{qq} of Eq. (10). For simplicity, it is assumed in this paper that the airfoil does not disturb the background flow, which is assumed to be constant and uniform, i.e., $U_0=U$.

Neglecting viscous stresses, the ith component of force acting on the fluid per unit area by the airfoil is given by

$$f_i(\mathbf{y},\tau)=-n_i(\mathbf{y})p_t(\mathbf{y},\tau), \tag{4}$$

where $n_i(\mathbf{y})$ is the ith component of the unit inward normal $\mathbf{n}(\mathbf{y})$ on the airfoil surface S, and p_t is the total aerofoil surface pressure, which includes the effect of the trailing edge. Volume-quadrupole sources generated by shear stresses in the boundary layer are assumed to be negligible compared with the dipole sources on the airfoil surface, although the proposed method has no difficulty in dealing with this quadrupole term in principle. For a rigid airfoil, the third term of the right-hand side of Eq. (1) represents a steady pressure, which does not radiate sound. Thus, we are only concerned with the second term of Eq. (1). Substituting the Green function of Eq. (2) into the second term of Eq. (1) and performing Fourier transformation with respect to t, gives the radiated pressure at a single frequency of the form,

$$\bar{p}(\mathbf{x},\omega)=\frac{1}{2\pi}\int_{-T}^{T}\iint_{S}[-n_i p_t(\mathbf{y},\tau)]\frac{\partial}{\partial y_i}\bar{G}(\mathbf{x},\mathbf{y},\omega)\,\mathrm{d}S(\mathbf{y})\mathrm{e}^{\mathrm{i}\omega\tau}\,\mathrm{d}\tau, \tag{5}$$

where the overbars are used to denote complex pressure amplitudes. Here, ω is the observed frequency related to time t at the observation point $\mathbf{x}$, and $\bar{G}$ is the Fourier transform of Eq. (2), given by

$$\bar{G}(\mathbf{x},\mathbf{y},\omega)=\frac{1}{4\pi R}\mathrm{e}^{\mathrm{i}\mu[R+M(y_1-x_1)]}, \tag{6}$$

where $\mu=\kappa/\beta^2$, and $\kappa=\omega/c_0$ is acoustic wavenumber related to the observer frequency ω. We now consider the computation of the total surface pressure distribution, p_t, on the airfoil surface resulting from the interaction of the hydrodynamic boundary layer pressure field with the trailing edge.

4. Spectra of "incident" boundary layer pressure

Following the philosophy of Chase [2] and Amiet [1] for making trailing edge noise predictions, it is convenient to use as input data the surface boundary layer pressures measured well away from the trailing edge. This distance, as demonstrated by Ffowcs Williams and Hall [9] and Brooks and Hodgson [10], is approximately one hydrodynamic wavelength from the trailing edge. The scattered pressure p_s may be obtained from p_i by imposing the Kutta condition, such that the incident and scattered pressures exactly cancel at the trailing edge. Once the relationship between p_i and p_s is established, the problem of broadband self-noise prediction is therefore completely determined from the spectral characteristics of the incident pressure.

The unsteady wall pressure, $p_i(\mathbf{y},\tau)$, due to turbulence incident upon the trailing edge, can be written in terms of its wavenumber–frequency components $\hat{p}_i(\mathbf{k},\omega_0)$ by the Fourier Transform relation

$$p_i(\mathbf{y},\tau)=\tilde{p}_i(\boldsymbol{\eta},\tau)=\int_{-\infty}^{\infty}\int_{-\infty}^{\infty}\int_{-\infty}^{\infty}\hat{p}_i(\mathbf{k},\omega_0)\mathrm{e}^{\mathrm{i}(\mathbf{k}\cdot\boldsymbol{\eta}-\omega_0\tau)}d^2\mathbf{k}\mathrm{d}\omega_0, \tag{7}$$

where $\mathbf{k}=(k_s,\ k_t)$, $\boldsymbol{\eta}=(\eta_s,\ \eta_t)=\boldsymbol{\eta}(\mathbf{y})$, ω_0 is the angular frequency. Fourier components $\hat{p}_i(\mathbf{k},\omega_0)$ can be determined from $\tilde{p}_i(\boldsymbol{\eta},\tau)$ by the inverse relation,

$$\hat{p}_i(\mathbf{k},\omega_0)=\frac{1}{(2\pi)^3}\int_{-\infty}^{\infty}\int_{-\infty}^{\infty}\int_{-\infty}^{\infty}\tilde{p}_i(\boldsymbol{\eta},\tau)\mathrm{e}^{-i(\mathbf{k}\cdot\boldsymbol{\eta}-\omega_0\tau)}d^2\boldsymbol{\eta}\mathrm{d}\tau. \tag{8}$$

For broadband problems, it is useful to work with pressure wavenumber–frequency spectral densities. For simplicity, we assume here that the turbulent pressure field is spatially homogeneous and stationary with respect to time, i.e. the space-time correlations of the boundary layer pressure field are dependent only on the separation distance and temporal interval. Under this assumption, the wall-pressure $\hat{p}_i(\mathbf{k},\omega_0)$ at different frequencies and wavenumbers are uncorrelated and the frequency–wavenumber spectral density $S_{qq}(\mathbf{k},\omega_0)$ of the boundary layer pressure is given by

$$E\left[\hat{p}_i^*(\mathbf{k},\omega_0)\hat{p}_i\left(\mathbf{k}',\omega_0'\right)\right]=\delta(\mathbf{k}'-\mathbf{k})\delta\left(\omega_0'-\omega_0\right)S_{qq}(\mathbf{k},\omega_0), \tag{9}$$

where the superscript "*" denotes complex conjugation, $E[\ldots]$ denotes the expected value.

The surface pressure boundary layer spectrum is dominated by pressure contributions in the convective region [11] in which turbulent eddies convect at speeds slower than the speed of sound. In the absence of the trailing edge, therefore, the boundary layer pressure is weakly radiating. Howe [11] has surveyed various expressions for the frequency–wavenumber spectra of the turbulent boundary layer pressure on a flat plate. Chase [12] has developed an empirical formula for turbulent pressure spectra with adjustable constants that can be fixed by comparison with experimental data. A particularly simple form for the boundary layer spectrum was proposed by Corcos [13] as the product of independent separable functions of frequency and wavenumber of the form,

$$S_{qq}(\mathbf{k},\omega_0)=S_0(\omega_0)S_1(k_s)S_2(k_t), \tag{10}$$

where S_0 is the boundary layer frequency spectrum, and S_1 and S_2 are the wavenumber spectra in the streamwise and transverse directions respectively, given by

$$S_1(k_s) = \frac{l_1}{\pi}\left[\frac{1}{1 + l_1^2(\omega_0/U_c - k_s)^2}\right], \quad S_2(k_t) = \frac{l_2}{\pi}\left[\frac{1}{1 + l_2^2 k_t^2}\right], \tag{11,12}$$

where l_1 and l_2 are the respective boundary layer integral length-scales. If the convection speed U_c is assumed to be constant, data obtained from experiments performed by Brooks and Hodgson [10] gives $l_1 = U_c/(0.11\omega_0)$ and $l_2 = U_c/(0.6\omega_0)$. The separable form is the most convenient for use in airfoil noise predictions as it allows the use of measured pressure spectra, and is the one adopted here. In this paper, we use the pressure frequency spectrum $S_0(\omega_0)$ presented in the book by Howe [11], based on data collated by Chase [12] for an infinite flat plate. In non-dimensional form, it is given by

$$\tilde{S}_0(\tilde{\omega}_0) = \frac{6.1409 \times 10^{-6}\tilde{\omega}_0^2}{(\tilde{\omega}_0^2 + 0.0144)^{1.5}}, \tag{13}$$

where $\tilde{S}_0(\tilde{\omega}_0) = S_0(\omega_0)(U_0/\delta^*)/(0.5\rho_0 U_0^2)^2$, $\tilde{\omega}_0 = \omega_0\delta^*/U_0$ (Strouhal number with respect to δ^*), and δ^* is the displacement thickness of the turbulent boundary layer, ρ_0 is the density of the steady background flow. The calculation of the displacement thickness δ^* as a function of chord length, angle of attack and flow speed were made using the empirical formula based on measured data by Brooks et al. [14] on a NACA 0012 airfoil.

A substantial simplification of the boundary layer spectrum, and hence of the final expression for the radiated noise spectrum, may be obtained by making the assumption that turbulence convects as a frozen pattern at the convection velocity U_c. For frozen boundary layer turbulence, $l_1 \to \infty$, which in Eq. (11) leads to $S_1(k_s) \to \delta(k_s - \omega_0/U_c)$. In this limit the incident wall pressure spectrum of Eq. (10) may be written as [8]

$$\hat{S}_{qq}(\mathbf{k}) = \int_{-\infty}^{\infty} S_{qq}(\mathbf{k}, \omega_0)\,\mathrm{d}\omega_0 = U_c S_0(k_s U_c) S_2(k_t). \tag{14}$$

The characteristics of the boundary layer turbulence on an airfoil differ from that on a flat plate in three important respects: (i) the boundary layer thickness grows along the streamwise direction; (ii) local incoming velocity U_0 is non-uniform due to potential flow effects; (iii) there is a pressure gradient in the streamwise direction within the boundary layer. We assume here that the boundary layer thickness, the incoming velocity and the pressure gradient are uniform over a small facet of the airfoil surface so that the pressure spectrum of Eq. (10) remains locally valid. We further assume that an aerofoil with the same local inflow velocity $U_0(\mathbf{y})$, and boundary layer thickness $\delta^*(\mathbf{y})$ develops the same pressure frequency–wavenumber spectrum as a flat plate under the same conditions. The Corcos model of the pressure spectrum will therefore be extended to realistic airfoil geometries by applying it locally to a small region on the airfoil surface, which is small compared with an acoustic and hydrodynamic wavelength. From Eq. (7), a single frequency–wavenumber component of the incident boundary layer surface pressure can be written as

$$p_i(\mathbf{y}, \tau) = \bar{p}_i(\mathbf{y}, \omega_0)\mathrm{e}^{-\mathrm{i}\omega_0\tau}, \quad \bar{p}_i(\mathbf{y}, \omega_0) = \hat{p}_i(\mathbf{k}, \omega_0)\mathrm{e}^{\mathrm{i}\mathbf{k}\cdot\boldsymbol{\eta}}. \tag{15a,15b}$$

As pointed out by Amiet [15], the use of Eq. (15) to represent the boundary layer pressure suggests that it appears suddenly at the aerofoil leading edge, which is non-physical. A more physically realistic representation of the incident pressure would be one in which it increased gradually from zero at the leading edge, to reach its maximum value at the trailing edge, and which was identically zero further downstream. Accordingly, Amiet [15] introduces an exponential decay function $f_p = e^{-\varepsilon|k_s\eta_s|}$, which multiplies the right-hand side of Eq. (15), where ε is an arbitrary decay factor chosen to give the desired behaviour. Here, we choose another function f_p in a manner that is fully consistent with the surface pressure spectral predictions made locally on the aerofoil surface, which has the requisite behaviour of Amiet's decay function, but does not require the selection of an arbitrary constant. Here we define a position-dependent function in terms of pressure spectrum evaluated locally at position $\mathbf{y}$ on the airfoil surface,

$$f_p(\mathbf{y}, \mathbf{k}, \omega_0) = \sqrt{\frac{S_{qq}(\mathbf{y}, \mathbf{k}, \omega_0)}{S_{qq}(\mathbf{y}_0, \mathbf{k}, \omega_0)}}, \tag{16}$$

where $\mathbf{y}_0$ is a reference point chosen at the airfoil trailing edge. Note that f_p has the required behaviour, $f_p(\mathbf{y}_{LE}, \mathbf{k}, \omega_0) = 0$, for all $\mathbf{k}$ and ω_0, where $\mathbf{y}_{LE}$ is a point at the leading edge. A single spectral component of the incident surface pressure field of Eq. (15) can therefore be written as

$$p_i(\mathbf{y}, \tau) = f_p(\mathbf{y}, \mathbf{k}, \omega_0)\bar{p}_i(\mathbf{y}, \omega_0)\mathrm{e}^{-\mathrm{i}\omega_0\tau}. \tag{17}$$

5. Unsteady airfoil surface pressure

The relationship between an incident harmonic component of pressure p_i of the form given by Eq. (15) and the pressure difference $\Delta\bar{p}_s$ across a flat plate due to scattered pressure by the trailing edge of a two-dimensional flat plate airfoil was derived by Amiet [6]. His solution satisfies the linear Helmholtz equation, the Kutta condition at the trailing edge, and the no-flow condition on the blade surface. Note also that secondary scattering by the leading edge is assumed to be negligible in this paper. According to Roger and Moreau [17], the leading edge correction is only significant at low reduced frequency $\omega c/c_0 < 1$, where c is the chord length. Assuming a convection speed of $U_c = 0.65U_0$, at the peak of the hydrodynamic pressure spectrum the condition $\omega c/c_0 < 1$ implies a hydrodynamic wave length $\lambda_h > 4.08M_0c$. If we assume a Mach number, $M_0 = 0.1$, then $\lambda_h > 0.408c$. In this case the hydrodynamic wavelength λ_h is too long to be supported in the turbulent boundary layer and is therefore physically unreasonable. Roger's leading edge correction to the trailing edge solution is shown to be of second order in frequency compared to the first order trailing edge solution. Furthermore the trailing edge solution decays from trailing edge (see Fig. 3 in Roger's paper and Fig. 2 in this paper). The leading edge correction is therefore small compared to the principal trailing edge term except in cases such as in underwater examples where the Mach number is small. In this paper, Roger's leading edge correction is therefore ignored. Following the approach first proposed by Amiet, his original two-dimensional solution in Ref. [6] is extended here to allow for wavenumber components of boundary layer pressure arriving at oblique angles to the trailing edge [8]. The result has been used to define a transfer function H_s that relates the pressure jump $\Delta\bar{p}_s$ to a single wavenumber component of pressure $\bar{p}_i$ incident upon the trailing edge,

$$\Delta\bar{p}_s(\mathbf{y}, \omega_0) = H_s(\mathbf{y}, \mathbf{k}, \omega_0)\bar{p}_i(\mathbf{y}, \omega_0), \tag{18}$$

where H_s is given by

$$H_s(\mathbf{y}, \mathbf{k}, \omega_0) = \mathrm{erf}\left(\sqrt{\mathrm{i}(K + \mu_0 M_0 + k_s)\eta_s}\right) - 1, \tag{19}$$

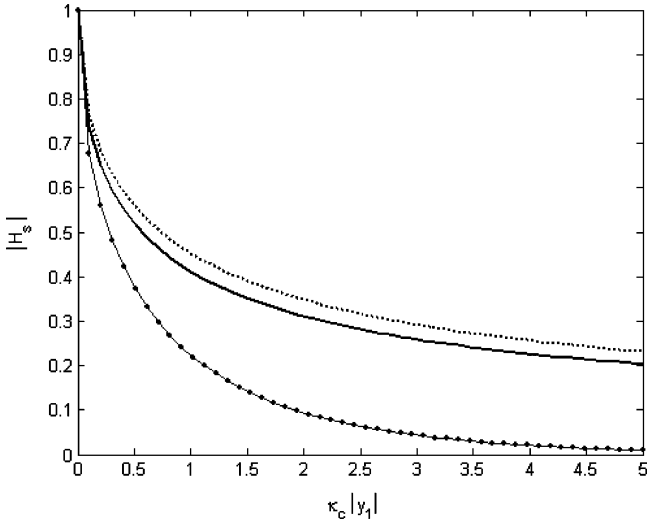

Fig. 2. Modulus of the transfer function H_s vs. dimensionless distance $\kappa_c\ |y_1|$ for various normalized spanwise wavenumber $k_t\beta_0/\kappa_0$, ——— $k_t\beta_0/\kappa_0 = 0$, ▪▪▪▪▪▪ $k_t\beta_0/\kappa_0 = 1.0$, —●— $k_t\beta_0/\kappa_0 = 2.0$.

and where erf(⋯) denotes the error function, $K=\sqrt{\mu_0^2-(k_t/\beta_0)^2}$, $\mu_0=\kappa_0/\beta_0^2$, $\kappa_0=\omega_0/c_0$ is the acoustic wavenumber related to the source frequency ω_0, c_0 is the speed of sound, and $M_0=U_c/c_0$ is the Mach number related to the airfoil velocity, $\beta_0=\sqrt{1-M_0^2}$. Eqs. (18) and (19) are consistent with the two-dimensional solution formulated by Amiet [6] for $k_t=0$ (with the sign of μ_0 and k_s changed due to Amiet's choice of time convention, $e^{i\omega\tau}$), and reduces to the solution given by Howe [5] for $M_0=0$. Fig. 2 shows $|H_s|$ plotted against dimensionless distance, $\kappa_c|y_1|$, from the trailing edge for the normalized spanwise wavenumber, $k_t\beta_0/\kappa_0=0.0$, 1.0, 2.0, where $\kappa_c=\omega_0/U_c$. Fig. 2 shows that $|H_s|$ decays rapidly with distance from the trailing edge. This finding suggests that the equivalent sources for trailing edge noise are predominantly located close to the trailing edge and generated by boundary layer wavenumber components arriving at angle close to normal incidence to the trailing edge.

Eq. (18) relates to the pressure differential produced across the surface of a flat plate airfoil. For more realistic aerofoil geometries, numerical methods such as the boundary element method may be used to obtain more accurate solutions for H_s. However, the use of flat plate theory is anticipated to provide a good approximation to the surface pressures generated by trailing edge interaction since the aerodynamic sources are mostly confined to the trailing edge where the airfoil is thinnest and most closely approximates to a flat plate. We further make the assumption of high-reduced frequency $\sigma_1=\kappa_c b$ (b is the airfoil semi-chord), where the hydrodynamic wavelength of turbulence is much smaller than the chord so that the leading edge correction due to the backward scattered pressure impinging on the leading edge can be neglected [16]. The wedge angle effect at airfoil trailing edge on the aerodynamic response function H_s is also ignored. The airfoil response function in this case can therefore be treated as a flat plate with chord equal to the arc length of the actual aerofoil. However, the effects of aerofoil geometry on sound radiation, taking into account retarded time effects, are included in the formulation by integrating over the actual blade surface.

Eqs. (18) and (19) refer to the pressure jump across the flat plate. Howe [5] has shown from a low Mach number approximation to the trailing edge problem that the magnitudes of the scattered pressure on each side of the flat plate airfoil are identical and equal to half the magnitude of the pressure jump $|\Delta\bar{p}_s|$, while the phase of the scattered pressures on the two sides differ by 180°. Taking into account the position-dependent function $f_p(\mathbf{y},\ \mathbf{k},\ \omega)$ in the definition of the incident pressure p_i according to Eq. (17), the total pressure p_t distributed over the surface of a real airfoil may therefore be approximated by

$$p_t(\mathbf{y},\tau)=\int_{-\infty}^{\infty}\int_{-\infty}^{\infty}\int_{-\infty}^{\infty}H_q(\mathbf{y},\mathbf{k},\omega_0)\hat{p}_i(\mathbf{k},\omega_0)e^{i(\mathbf{k}\cdot\boldsymbol{\eta}-\omega_0\tau)}d^2\mathbf{k}\,d\omega_0, \tag{20}$$

where H_q is the transfer function between the surface pressure at any point on the airfoil surface $\boldsymbol{\eta}=(\eta_s,\ \eta_t)$ and a single wavenumber component of incident boundary layer pressure evaluated at the reference point y_0 along the trailing edge, of the form,

$$H_q(\mathbf{y},\mathbf{k},\omega_0)=\begin{cases} f_p(\mathbf{y},\mathbf{k},\omega_0)+\frac{1}{2}H_s(\mathbf{y},\mathbf{k},\omega_0), & \mathbf{y}\text{ on the turbulence side,}\\ -\frac{1}{2}H_s(\mathbf{y},\mathbf{k},\omega_0), & \mathbf{y}\text{ not on the turbulence side.}\end{cases} \tag{21}$$

6. Airfoil broadband self-noise prediction

The time-harmonic analysis of Eq. (5) is now generalized to the case of a turbulent boundary layer pressure incident on the trailing edge from one side of the airfoil. Substituting Eq. (20) into Eq. (5) and carrying out the integration with respect to τ and ω_0, the expression for the radiated pressure becomes

$$\bar{p}(\mathbf{x},\omega)=\int_{-\infty}^{\infty}\int_{-\infty}^{\infty}H_p(\mathbf{x},\mathbf{k},\omega)\hat{p}_i(\mathbf{k},\omega)\,d^2\mathbf{k}, \tag{22}$$

where H_p is a radiation transfer function relating the radiated pressure at point $\mathbf{x}$ in the radiation field to each wavenumber component $\mathbf{k} = (k_s, k_t)$ of pressure on the airfoil surface, and takes the form

$$H_p(\mathbf{x}, \mathbf{k}, \omega) = -\iint_S H_q(\mathbf{y}, \mathbf{k}, \omega) e^{i\mathbf{k}\cdot\boldsymbol{\eta}} n_i(\mathbf{y}) \frac{\partial}{\partial y_i} \bar{G}(\mathbf{x}, \mathbf{y}, \omega) dS(\mathbf{y}), \tag{23}$$

where from Eq. (6),

$$\frac{\partial}{\partial y_1} \bar{G}(\mathbf{x}, \mathbf{y}, \omega) = \left[-\frac{y_1 - x_1}{R^2} + i\mu\left(\frac{y_1 - x_1}{R} + M\right)\right] \bar{G}(\mathbf{x}, \mathbf{y}, \omega) \tag{24}$$

and for $i = 2, 3$,

$$\frac{\partial}{\partial y_i} \bar{G}(\mathbf{x}, \mathbf{y}, \omega) = \left[-\frac{\beta^2}{R} + i\kappa \right] \frac{y_i - x_i}{R} \bar{G}(\mathbf{x}, \mathbf{y}, \omega), \quad (i = 2, 3). \tag{25}$$

The power spectral density of the pressure at position $\mathbf{x}$ is given by

$$S_{pp}(\mathbf{x}, \omega')\delta(\omega' - \omega) = E[\bar{p}^*(\mathbf{x}, \omega')\bar{p}(\mathbf{x}, \omega)]. \tag{26}$$

Substituting Eq. (22) into Eq. (26) and making use of Eq. (9) for the case of homogenous turbulence, the pressure spectrum at any field point $\mathbf{x}$ may be written as

$$S_{pp}(\mathbf{x}, \omega) = \int_{-\infty}^{\infty} \int_{-\infty}^{\infty} \left| H_p(\mathbf{x}, \mathbf{k}, \omega) \right|^2 S_{qq}(\mathbf{k}, \omega) \, d^2\mathbf{k}. \tag{27}$$

For frozen boundary layer turbulence, $S_1(k_s) \to \delta(k_s - \omega_0/U_c)$ as $l_1 \to \infty$ [8], which in Eq. (27) gives

$$S_{pp}(\mathbf{x}, \omega) = \frac{1}{U_c} \int_{-\infty}^{\infty} \left| H_p(\mathbf{x}, \omega/U_c, k_t, \omega) \right|^2 \hat{S}_{qq}(\omega/U_c, k_t) \, dk_t. \tag{28}$$

Since the effect of attack angle is incorporated into the formulation through the spectrum of incident boundary layer pressure of Eq. (10) and the position-dependent function $f_p(\mathbf{y}, \mathbf{k}, \omega)$ of Eq. (16), Eqs. (27) and (28) are valid, not only for flat plates with zero angle of attack, but also for an airfoil of arbitrary geometry with non-zero attack angle providing that boundary layer separation does not occur and that the trailing edge is sufficiently sharp on the scale of a hydrodynamic wavelength. Moreover, the solution is valid in both near and far fields. It is shown in Ref. [8] to reduce to Amiet's analytic solution [1] when the airfoil collapses to a flat plate with large span and the measurement point is taken to the far field.

7. Numerical scheme for the evaluation of the transfer function H_p

A numerical scheme is now presented for performing the calculation of H_p for arbitrary airfoil geometries. It is based on the observation that the hydrodynamic wavelength of the boundary layer turbulence is generally smaller than the acoustic wavelength. The integration of Eq. (23) is then split into two parts. One is a radiation term; the other is related to the hydrodynamic source term. The advantages of this separation are that it allows the hydrodynamic term to be integrated analytically over a small element facet of airfoil surface thereby improving considerably the efficiency of the computation.

In order to carry out the numerical calculation of Eq. (23) for arbitrary airfoil geometries, the airfoil surface is discretized into finite triangular elements. Assuming that, at a single frequency, each element $n (n = 1, 2, 3, \ldots, N_{ef})$ is small compared with the acoustic wavelength and that the position-dependent function $f_p(\mathbf{y}, \mathbf{k}, \omega)$ and $n_i(\mathbf{y})\partial\bar{G}/\partial y_i$ can be taken to be uniform within that element, Eq. (23) may be approximated by

$$H_p(\mathbf{x}, \mathbf{k}, \omega) = \sum_{n=1}^{N_{ef}} g_n(\mathbf{x}, \mathbf{y}_n, \omega) h_n(\mathbf{y}_n, \mathbf{k}, \omega), \tag{29}$$

where N_{ef} is the total number of elements. The radiation term g_n in Eq. (23), is given by

$$g_n(\mathbf{x}, \mathbf{y}_n, \omega) = N_n^i(\mathbf{y}_n) \frac{\partial}{\partial y_i} \bar{G}(\mathbf{x}, \mathbf{y}_n, \omega), \tag{30}$$

where $N_n^i = -n_i$ and $\mathbf{y}_n$ are the unit outward normal vector and the centre coordinates of the element n, respectively. From Eqs. (23) and (29), the term h_n is defined by

$$h_n(\mathbf{y}_n, \mathbf{k}, \omega) = \iint_{S_n} H_q(\mathbf{y}, \mathbf{k}, \omega) \mathrm{e}^{\mathrm{i}\mathbf{k}\cdot\boldsymbol{\eta}} \, \mathrm{d}S(\mathbf{y}). \tag{31}$$

Eqs. (10), (13) and (16) indicate that the position-dependent function $f_p(\mathbf{y}, \mathbf{k}, \omega)$ appearing in the definition of H_q of Eq. (21) mainly depends on the boundary layer thickness. The function $f_p(\mathbf{y}, \mathbf{k}, \omega)$ is slowly varying compared to variations in the incident boundary layer surface pressure. When the dimensions of the element S_n are sufficiently small compared to the airfoil chord, $f_p(\mathbf{y}, \mathbf{k}, \omega)$ can be taken out of the surface integration and the integral of Eq. (31) can be performed analytically. For this purpose we substitute Eqs. (19) and (21) into Eq. (31), and split the result into two parts:

$$h_n(\mathbf{y}_n, \mathbf{k}, \omega_0) = \begin{cases} \frac{1}{2} h_n^{(1)}(\mathbf{k}, \omega_0) + \left[f_p(\mathbf{y}_n, \mathbf{k}, \omega_0) - \frac{1}{2} \right] h_n^{(2)}(\mathbf{k}), & \mathbf{y}_n \text{ on turbulence side,} \\ -\frac{1}{2} [h_n^{(1)}(\mathbf{k}, \omega_0) - h_n^{(2)}(\mathbf{k})], & \mathbf{y}_n \text{ not on turbulence side.} \end{cases} \tag{32}$$

where $h_n{}^{(1)}$ and $h_n{}^{(2)}$ are given by

$$h_n^{(1)}(\mathbf{k}, \omega_0) = \iint_{S_n} \mathrm{erf}(\sqrt{a\eta_s}) \mathrm{e}^{i\mathbf{k}\cdot\boldsymbol{\eta}} \, \mathrm{d}^2\boldsymbol{\eta}, \quad h_n^{(2)}(\mathbf{k}) = \iint_{S_n} \mathrm{e}^{\mathrm{i}\mathbf{k}\cdot\boldsymbol{\eta}} \, \mathrm{d}^2\boldsymbol{\eta}, \tag{33a,b}$$

and where $a = \mathrm{i}(K + \mu_0 M + k_s)$. The numerical scheme described above is now applied to the triangular element S_n on the airfoil surface, expressed in curvilinear coordinates $\eta = (\eta_s, \eta_t)$, as sketched in Fig. 3.

The apexes of the triangle are $B(\eta_{sB}, \eta_{tB})$, $C(\eta_{sC}, \eta_{tC})$, and $D(\eta_{sD}, \eta_{tD})$. The triangular element S_n is meshed with one edge parallel to the η_s-axis, as shown in Fig. 3. The equation of any edge of the triangle, for example the line CD, may be written as

$$\eta_s^{CD} = p^{CD} \eta_t^{CD} + q^{CD}, \tag{34}$$

where the constants p^{CD} and q^{CD} can be determined by the coordinates of the points $C(\eta_{sC}, \eta_{tC})$, and $D(\eta_{sD}, \eta_{tD})$ on the line CD, using

$$p^{CD} = (\eta_{sD} - \eta_{sC})/(\eta_{tD} - \eta_{tC}), \quad q^{CD} = -p^{CD}\eta_{tC} + \eta_{sC}. \tag{35a,b}$$

The line CB is also described by Eqs. (34) and (35) with the superscript CD replaced by CB, and the subscript D replaced by B. With the above notation, the integration of Eq. (33a) can be performed analytically to give

$$\begin{aligned} h_n^{(1)}(\mathbf{k}, \omega_0) = {} & F(a, p^{CB}, q^{CB}, \eta_{tD}, \mathbf{k}, \omega_0) - F(a, p^{CB}, q^{CB}, \eta_{tC}, \mathbf{k}, \omega_0) \\ & - F(a, p^{CD}, q^{CD}, \eta_{tD}, \mathbf{k}, \omega_0) + F(a, p^{CD}, q^{CD}, \eta_{tC}, \mathbf{k}, \omega_0). \end{aligned} \tag{36}$$

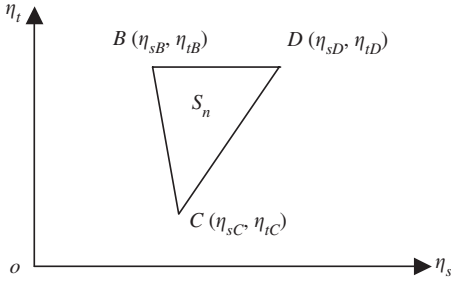

Fig. 3. A triangle element S_n with apexes BCD.

The function F, for $k_s \neq 0$, takes the following different forms depending on the values of p and k_t:

$$F(a,p,q,\eta_t,\mathbf{k},\omega_0)=\begin{cases}\dfrac{1}{\mathrm{i}pk_s}\mathrm{e}^{-\mathrm{i}k'_t q}\left[I(a,k_{st},\eta_s)-\sqrt{\dfrac{a}{k_a}}I(k_a,k'_t,\eta_s)\right], & p\neq 0,\ \ k_t\neq 0,\\ \dfrac{1}{\mathrm{i}k_s}\mathrm{e}^{-\mathrm{i}k_t\eta_t}I(a,k_s,\eta_s), & p=0,\ \ k_t\neq 0,\\ \dfrac{1}{\mathrm{i}pk_s}\mathrm{e}^{-\mathrm{i}k'_t q}\left[I(a,k_s,\eta_s)-\sqrt{\dfrac{a}{k_a}}I_2(k_a,\eta_s)\right], & p\neq 0,\ \ k_t=0,\\ \eta_t I(a,k_s,\eta_s), & p=0,\ \ k_t=0,\end{cases} \tag{37}$$

where

$$I(a,k_s,\eta_s)=\int \mathrm{erf}\left(\sqrt{a\eta_s}\right)\mathrm{e}^{\mathrm{i}k_s\eta_s}\mathrm{d}\eta_s=\frac{1}{\mathrm{i}k_s}\left[\mathrm{erf}(\sqrt{a\eta_s})\mathrm{e}^{\mathrm{i}k_s\eta_s}-\sqrt{\frac{a}{k_a}}\mathrm{erf}(\sqrt{k_a\eta_s})\right], \tag{38}$$

$$I_2(k_a,\eta_s)=\int \mathrm{erf}\left(\sqrt{k_a\eta_s}\right)\mathrm{d}\eta_s=\left(\eta_s-\frac{1}{2k_a}\right)\mathrm{erf}\left(\sqrt{k_a\eta_s}\right)+\frac{1}{\sqrt{\pi k_a}}\sqrt{\eta_s}\mathrm{e}^{-k_a\eta_s}, \tag{39}$$

and $\eta_s = p\eta_t + q$, $k_a = a - \mathrm{i}k_s$, $k'_t = k_t/p$ and $k_{st} = k_s + k'_t$.

The integration of Eq. (33b) can be written in a similar form to Eq. (36),

$$\begin{aligned}h_n^{(2)}(\mathbf{k})=\big[&F(p^{CB},q^{CB},\eta_{tD},\mathbf{k})-F(p^{CB},q^{CB},\eta_{tC},\mathbf{k})\\&-F(p^{CD},q^{CD},\eta_{tD},\mathbf{k})+F(p^{CD},q^{CD},\eta_{tC},\mathbf{k})\big],\end{aligned} \tag{40}$$

where F is now given by

$$F(p,q,\eta_t,\mathbf{k})=\begin{cases}-\dfrac{1}{k_s(k_s p+k_t)}\mathrm{e}^{\mathrm{i}[k_s(p\eta_t+q)+k_t\eta_t]}, & p\neq 0,\ \ k_s\neq 0,\ \ k_t\neq 0,\\ -\dfrac{1}{k_s k_t}\mathrm{e}^{\mathrm{i}[k_s q+k_t\eta_t]}, & p=0,\ \ k_s\neq 0,\ \ k_t\neq 0,\\ -\mathrm{i}\dfrac{\eta_t}{k_s}\mathrm{e}^{\mathrm{i}k_s q}, & p=0,\ \ k_s\neq 0,\ \ k_t=0.\end{cases} \tag{41}$$

Example calculations using this prediction scheme are presented below.

8. Numerical results

In this section, the frequency domain formulations of Eqs. (27) and (28) will be applied to predict the self-noise radiated from a flat plate, and a NACA 0012 and NACA 0024 airfoil. The results are expressed as a sound pressure level (L_p), defined as the spectral density of mean square pressure in a 1 Hz bandwidth, in decibels relative to $p_{\mathrm{ref}} = 2\times 10^{-5}$ Pa,

$$L_p(\mathbf{x},f)=10\log_{10}\frac{4\pi S_{pp}(\mathbf{x},\omega)}{p_{\mathrm{ref}}^2}, \tag{42}$$

where $f=\omega/2\pi$ is the frequency in Hertz, and the factor 4π is included to convert from a double sided spectrum to a single sided ($0<\omega<\infty$) spectrum, and from radian frequency to Hertz. The directivity of the radiated sound field in decibels, defined here as

$$D(\Psi,\theta,f)=10\log_{10}\left[R_d^2\frac{4\pi S_{pp}(\mathbf{x},\omega)}{p_{\mathrm{ref}}^2}\right], \tag{43}$$

where $\mathbf{x}=(R_d\sin\theta\cos\Psi, R_d\cos\theta, R_d\sin\theta\sin\Psi)$ is the observer position, p and where (R_d, Ψ, θ) is a spherical coordinate system, as shown in Fig. 1. Here R_d is the observer distance from the origin, located at the mid-span point at the trailing edge, Ψ is the polar angle measured from the x_1-axis in the mid-span plane, and θ is the azimuthal angle measured from the x_2-axis.

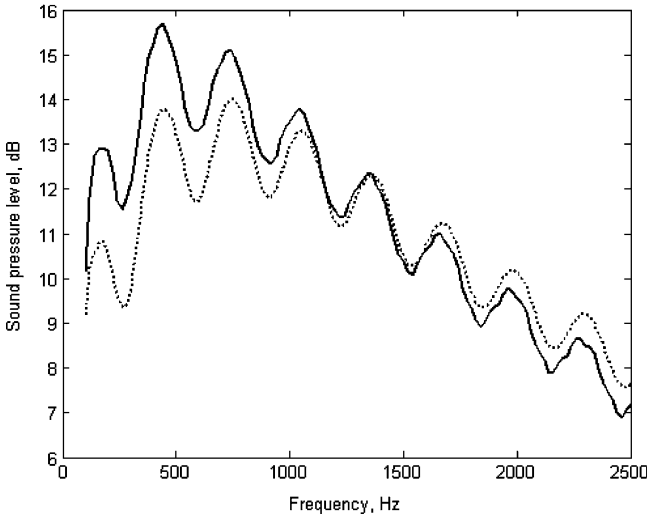

Fig. 4. Comparison of broadband self-noise prediction for a flat plate airfoil, decay factor $\varepsilon = 0.3$, Mach number $M = 0.3$, ▪▪▪▪▪▪ Amiet analytic solution, ▬▬▬ numerical method.

The use of Eqs. (27) and (28) to compute the radiated pressure spectrum S_{pp} assumes that the boundary layer turbulence on the airfoil suction side and pressure side are statistically independent. The spectra of radiated pressure due to the turbulence on each side are calculated separately and then added incoherently to obtain the total pressure spectrum at any observer position. The contribution to the radiated pressure due to the turbulence on each side of the airfoil is obtained by integrating the transfer functions of Eq. (23) over both the suction side and the pressure side.

8.1. Comparison of numerical predictions with Amiet's solution for a plate airfoil

The flat plate airfoil used for this prediction has a chord length of $2b = 1.0\,\text{m}$ and a span of $2d = 4.0\,\text{m}$, typical of a small aircraft wing. It moves in the $-y_1$ direction with Mach number $M = 0.3$. For the purpose of comparison with the analytic solution due to Amiet [1], the span is chosen to comply with his assumption of large span. The convective velocity coefficient of $c_u = 0.8$ is used. Fig. 4 shows a comparison between the broadband self-noise spectrum predicted using Amiet's solution [1] and the numerical solution for an observer at the mid-span plane of $\mathbf{x} = (0.0,\ 0.0,\ 150.0)\,\text{m}$.

In the low frequency range, $f < 800\,\text{Hz}$, the numerical prediction is typically 2 dB greater than that predicted using the analytic solution. At higher frequencies, agreement is better than 0.5 dB but then becomes worse as frequency is increased further. The discrepancy arises because Amiet makes the approximation that only $k_t = 0$ pressure component contributes to the radiation in the mid-span plane whereas the numerical result includes integration over all spanwise wavenumber k_t.

To establish the reason why the numerical result is not exactly identical to Amiet's solution we put $S_2(k_t) = \delta(k_t)$ in Eq. (14), consistent with Amiet's solution in the large-span limit for mid-span observers, and substitute it into Eq. (28) to give

$$S_{pp}(\mathbf{x}, \omega) = \left|H_p(\mathbf{x}, \omega/U_c, 0, \omega)\right|^2 S_0(\omega). \tag{44}$$

Amiet's analytic solution [18] can be rewritten in exactly the same form as Eq. (44)

$$S_{pp}(\mathbf{x}, \omega) = \left|H_{\text{Amiet}}(\mathbf{x}, \omega/U_c, 0, \omega)\right|^2 S_0(\omega). \tag{45}$$

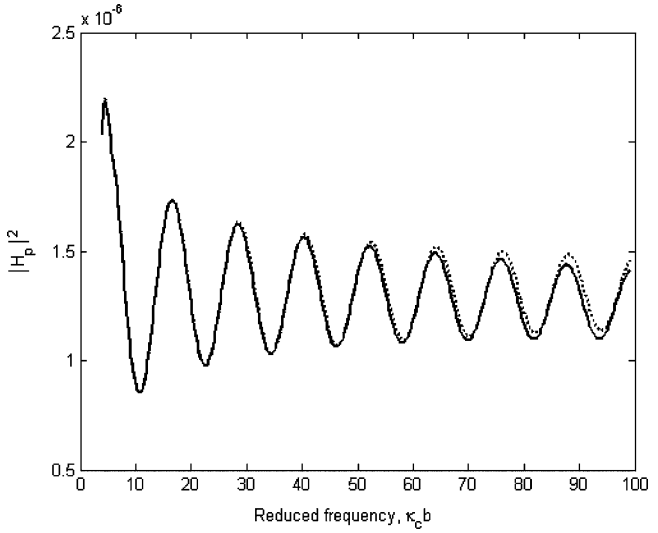

Fig. 5. Modulus squared transfer function $|H_p|^2$ vs. reduced frequency σ_1 for the flat plate airfoil of 1.0×4.0 m, $R_d = 150.0$ m, $\varepsilon = 0.3$, $M = 0.3$, ▪▪▪▪▪▪ Amiet analytic solution, ▬▬ numerical method.

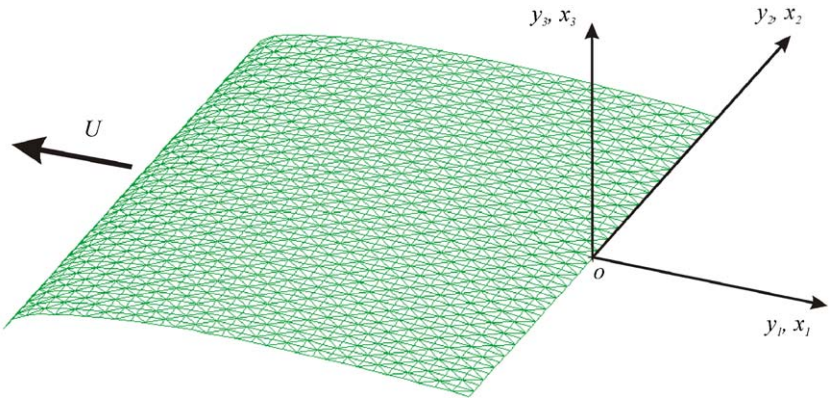

Fig. 6. Suction side mesh of the NACA 0012 airfoil for numerical calculation.

where the transfer function $|H_{\text{Amiet}}|^2$ may be expressed as

$$\left|H_{\text{Amiet}}(\mathbf{x}, k_1, 0, \omega)\right|^2 = \left[\frac{\kappa b x_3}{2\pi R_s^2}\right]^2 d^2 \left|L(\mathbf{x}, k_1, 0, \omega)\right|^2, \tag{46}$$

where $R_s = \sqrt{x_1^2 + \beta^2(x_2^2 + x_3^2)}$ and $L(\mathbf{x}, k_1, k_2, \omega) = \int_{-2}^{0} H_q(\mathbf{y}, k_1, k_2, \omega) \mathrm{e}^{\mathrm{i}k_1 b\xi} \mathrm{e}^{\mathrm{i}\mu b\xi(M - x_1/R_s)}\, \mathrm{d}\xi$. Note that for a single wave component with $k_2 = 0$, the surface pressure is coherent along the span so that the spanwise correlation length $l_y = d$ (for more discussion on Amiet's solution see Ref. [8]). Comparing Eq. (44) with Eq. (45), one may conclude that if $|H_p|^2$ of Eq. (23) is identical to $|H_{\text{Amiet}}|^2$ of Eq. (46), the numerical result of Eq. (44) and Amiet's solution of Eq. (45) are the same. The variation of $|H|^2$, defined in Eqs. (23) and (46), with reduced frequency $\sigma_1 = \kappa_c b$ is plotted in Fig. 5. The observation point is taken at $\mathbf{x} = (0.0, 0.0, 150.0)$ m. The dash line is obtained using Amiet's solution of Eq. (46) and the solid line obtained by the numerical method given by Eqs. (23) and (29). Fig. 5 confirms that the numerical results are identical to the Amiet's solution when the conditions are made the same.

Figs. 5 suggests that Amiet's solution is a reasonable approximation to the trailing edge noise due to flat plate airfoils with span large compared to the acoustic wavelength for far field observers. The largest errors are observed at high and low frequencies due to Amiet assumptions.

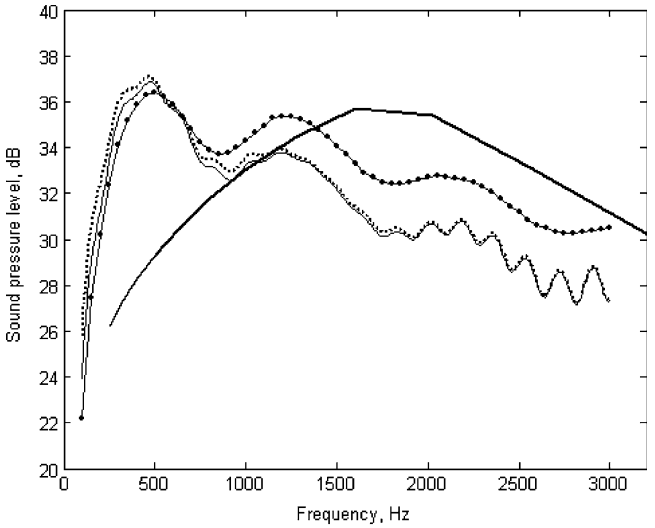

Fig. 7. Comparison of broadband self-noise with Brooks empirical prediction, ▬▬ Brooks formulation, ▪▪▪▪▪▪ frozen turbulence, full k_t range, —— frozen turbulence, supersonic k_t range, —●— non-frozen turbulence, supersonic k_t range.

8.2. Self-noise radiation from NACA airfoils

In this section, the theory presented above is used to predict the self-noise radiation from two NACA airfoils. These are then compared with predictions obtained using the empirical prediction method due to Brooks et al. [14]. The numerical method will first be applied to predict the self-noise radiation from one of the NACA 0012 airfoils investigated by Brooks. This airfoil has 0.3048 m chord, a span of 0.4752 m, and which moves in the $-y_1$ direction with Mach number $M = 0.208$ at an attack angle of $\alpha = 4^\circ$. A convective velocity coefficient of $c_u = 0.8$ is used. Fig. 6 presents the suction-side mesh of the NACA 0012 airfoil used for numerical calculation. Here we choose an element size $l_e = c_0/(10f) = 0.0115$ m, which is 10 times smaller than the acoustic wavelength for a mesh that is valid up to $f = 3000$ Hz. As shown in Fig. 6, this criterion corresponds to a mesh comprising 5952 triangle elements and 3038 nodes for the NACA 0012 airfoil used in the Brooks experiment with the dimensions given above.

8.2.1. Comparison of airfoil self-noise prediction scheme with the brooks method

Fig. 7 shows a comparison between self-noise predictions obtained using the empirical prediction scheme due to Brooks (solid curve) [14], and that predicted using the numerical scheme described above based on the following three assumptions:

(i) Non-frozen boundary layer $0 \leqslant k_s \leqslant \infty$, supersonic wavenumber components $0 \leqslant k_t \leqslant \kappa_0/\beta^2$.
(ii) Frozen boundary layer $k_s = \omega/U_c$, supersonic and subsonic wavenumber components $0 \leqslant k_t \leqslant \infty$ (upper limit chosen to ensure convergence).
(iii) Frozen boundary layer $k_s = \omega/U_c$, supersonic wavenumber components $0 \leqslant k_t \leqslant \kappa_0/\beta^2$.

The Brook's scheme is based on a regression analysis of the data obtained from an extensive experimental database of self-noise radiation measurements from a NACA 0012 airfoil. The measurements were made over a broad range of flow speeds, angles of attack and chord lengths. The prediction is made for the NACA 0012 airfoil described above, moving in the $-y_1$ direction with Mach number $M = 0.208$ at an attack angle of $\alpha = 4^\circ$. The observation point is at $\mathbf{x} = (0.0, 0.0, 1.22)$ m, for consistency with the Brooks experiment.

The numerical predictions are shown to be within 6 dB of the prediction obtained following Brooks et al. Note, however, that the Brooks prediction scheme applies to 1/3 octave bands only and cannot capture the details in the spectrum. Fig. 6 shows that the contributions from subsonic-k_t components become increasingly

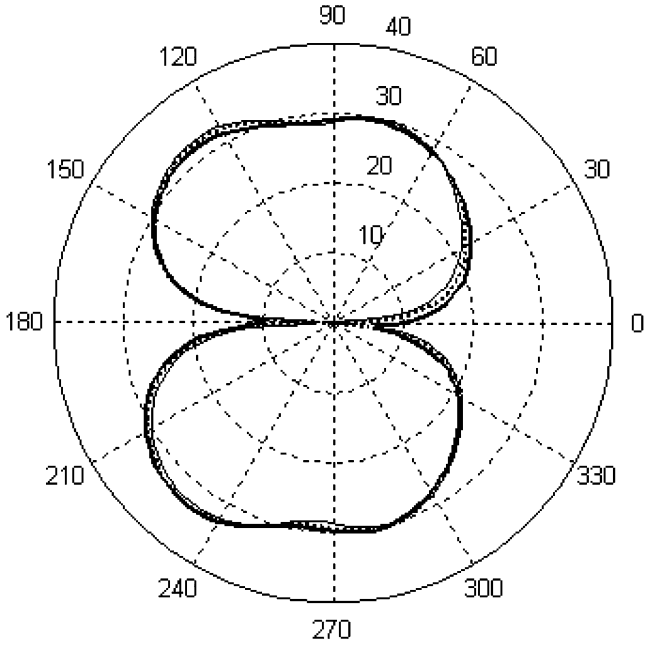

Fig. 8. Polar directivity (in Ψ-direction), $D(\Psi, \pi/2, \omega)$ −13.0 dB, of broadband noise for frozen incident turbulence, $M = 0.3$, —— flat plate, ▪▪▪▪▪▪ NACA 0012, ▬▬▬ NACA 0024.

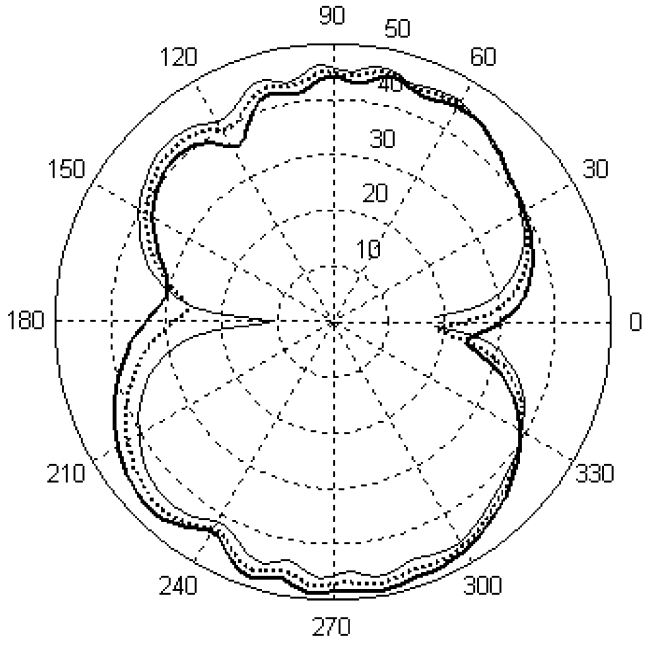

Fig. 9. Polar directivity (in Ψ-direction), $D(\Psi, \pi/2, \omega)$−13.0 dB, of broadband noise for frozen incident turbulence, $M = 0.8$, —— flat plate, ▪▪▪▪▪▪ NACA 0012, ▬▬▬ NACA 0024.

smaller as frequency increases. It also suggests that the frozen turbulence assumption gives a better approximation at low frequency than at high frequency. The difference in the self-noise prediction between the frozen and non-frozen gust assumptions is about 2 dB at high frequencies. Thus, the frozen-turbulence assumption appears to be reasonably valid for making airfoil self-noise predictions.

8.2.2. Broadband self-noise directivity and the effect of airfoil geometry

The broadband self-noise directivity and the effect of airfoil geometry on self-noise radiation are now investigated. Figs. 8 and 9 present the polar directivities of broadband self-noise, $D(\Psi, \pi/2, \omega)$, evaluated in the mid-span plane, for a flat plate, and a NACA 0012 and a NACA 0024 airfoil at Mach numbers of $M = 0.3$ and $M = 0.8$, respectively. The calculation is based on $R_d = 10.0\,\mathrm{m}$, $f = 1042.8\,\mathrm{Hz}$, and $\alpha = 4^\circ$. The directivities for the NACA 0024 airfoil, the NACA 0012 airfoil, and the flat plate are represented by the dark solid line, the dotted line and the solid line, respectively. All airfoil geometries have the same chord of $c = 0.3048\,\mathrm{m}$ and span of $2d = 0.4752\,\mathrm{m}$.

The directivity patterns exhibit asymmetric behaviour due to the non-zero angle of attack assumed in these examples. In contrast with the single wavenumber directivity functions, the broadband directivity functions vary very slowly with polar angle. Fig. 8 indicates that airfoil geometry does not alter appreciably the directivity pattern at low Mach number. The greatest difference is observed to occur at radiation angles close to the airfoil chord direction, $\Psi = 0$, π. This effect is most pronounced at high Mach number, where at $M = 0.8$ differences of up to 20 dB are observed.

The reason why the thickness effect is significant at high Mach number in the airfoil chord direction is due to unit normal vector component $n_1 \neq 0$. For a flat plate airfoil, the contribution due to $n_1(\partial/\partial y_1)\bar{G}$ in Eqs. (23) and (24) is zero since $n_1 = 0$. A significant contribution only arises due to the term $n_3(\partial/\partial y_3)\bar{G}$ in Eqs. (23) and (25). If $R \gg 1$ for far field observers, Eqs. (24) and (25) can be approximated by

$$\frac{\partial}{\partial y_1}\bar{G} \approx \mathrm{i}\frac{1}{\beta^2}\left(-\frac{x_1}{R} + M\right)\kappa\bar{G} \propto \frac{1}{\beta^2}\left(-\frac{x_1}{R} + M\right), \tag{47}$$

$$\frac{\partial}{\partial y_3}\bar{G} \approx -\mathrm{i}\frac{x_3}{R}\kappa\bar{G} \propto -\frac{x_3}{R}. \tag{48}$$

Considering a NACA 0024 airfoil, we have $n_1 \approx 0.248$ and $n_3 \approx 0.969$ near the trailing edge. When the airfoil move at $M = 0.8$ as for the case of Fig. 9, one has $n_1(\partial/\partial y_1)\bar{G} \gg n_3(\partial/\partial y_3)\bar{G}$ in the airfoil chord direction (with negative x_1). Therefore, the contribution due to airfoil thickness cannot be ignored at high Mach number in the airfoil chord direction. The thickness to acoustic wavelength ratio for the NACA 0024 airfoil is 0.24 in both cases of Figs. 8 and 9. The thickness to hydrodynamic wavelength ratio of boundary layer turbulence is

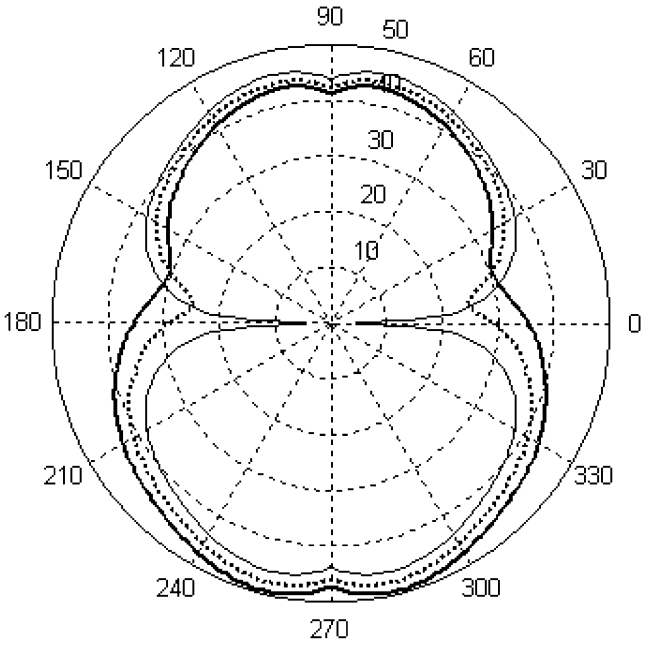

Fig. 10. Azimuthal directivity, $D(\pi/2, \theta, \omega)$ −15 dB, of broadband self-noise (in θ-direction) for frozen incident turbulence, $\sigma_1 = 12.13$, —— $\Psi = 90^\circ$, flat plate, ▪▪▪▪▪▪ $\Psi = 90^\circ$, NACA 0012, ▬▬ $\Psi = 90^\circ$, NACA 0024.

1.0 in the case of Fig. 8, while in the case of Fig. 9 this thickness ratio is only 0.37 (convective velocity coefficient of $c_u = 0.8$ assumed). However, the difference in noise radiation due to thickness effect in the case of Fig. 8 is weaker than in the case of Fig. 9. This indicates that the thickness effect mainly depends on the term $n_1(\partial/\partial y_1)\bar{G}$ in Eq. (23), which Amiet's theory has ignored through the assumption of a flat plate airfoil, rather than the term due to hydrodynamic source $H_q(\mathbf{y}, \mathbf{k}, \omega)e^{i\mathbf{k}\cdot\boldsymbol{\eta}}$.

Consider now the directivity pattern at an arbitrary position away from mid-span plane ($\theta \neq \pi/2$). Fig. 10 presents the self-noise directivity $D(\pi/2, \theta, \omega)$ in the azimuthal plane $\Psi = \pi/2$ for a flat plate, and a NACA 0012 and a NACA 0024 airfoil at the Mach number of $M = 0.8$. Fig. 10 suggests that the effect of airfoil thickness is significant at high Mach number. The largest differences are observed in the direction near the spanwise direction ($\theta \approx 0, \pi$). The computation parameters used to calculate Fig. 10 are identical to those in Fig. 9.

9. Conclusion

A numerical approach, based in the frequency domain, has been described for making airfoil self-noise predictions. It is valid for arbitrary airfoil geometries at small, but non-zero, angles of attack. Moreover, the solution is valid in both near and far fields and reduces to Amiet's analytic solution when the airfoil collapses to a flat plate with large span and the measurement point is taken to the far field. Numerical predictions of broadband self-noise have been shown to be within 6 dB of the prediction obtained using the Brooks empirical prediction scheme. Broadband self-noise predictions are made for both frozen and non-frozen boundary layer turbulence. The assumption of non-frozen turbulence is shown to predict higher noise radiation than when the frozen turbulence assumption is made. The effect is most pronounced at high frequency although the difference is generally less than 3 dB, suggesting that the frozen-gust assumption is reasonably valid for broadband noise predictions. Broadband noise directivity has been predicted for a flat-plat, a NACA 0012 and a NACA 0024 airfoil. It is shown that Mach number has an important influence, not only on the magnitude of the broadband self-noise radiation, but also the directivity.

References

[1] R.K. Amiet, Noise due to turbulence flow past a trailing edge, *Journal of Sound and Vibration* 47 (3) (1976) 387–393.
[2] D.M. Chase, Sound radiated by turbulent flow off a rigid half-plane as obtained from a wavenumber spectrum of hydrodynamic pressure, *Journal of the Acoustical Society of America* 52 (1972) 1011–1022.
[3] K.L. Chandiramani, Diffraction of evanescent waves with applications to aerodynamically-scattered sound and radiation from unbaffled plates, *Journal of the Acoustical Society of America* 55 (1974) 19–29.
[4] D.M. Chase, Noise radiated from an edge in turbulent flow, *AIAA Journal* 13 (1975) 1041–1047.
[5] M.S. Howe, Trailing edge noise at low Mach numbers, *Journal of Sound and Vibration* 225 (2) (1999) 211–238.
[6] R.K. Amiet, High frequency thin-airfoil theory for subsonic flow, *AIAA Journal* 14 (8) (1976) 1076–1082.
[7] M.E. Goldstein, *Aeroacoustics*, McGraw-Hill Book Company, New York, 1976.
[8] Q. Zhou, A model for rotor broadband noise prediction, *PhD thesis*, ISVR, University of Southampton, UK, 2004.
[9] J.E. Ffowcs Williams, L.H. Hall, Aerodynamic sound generation by turbulence flow in the vicinity of a scattering half plane, *Journal of Fluid Mechanics* 40 (1970) 657–670.
[10] T.F. Brooks, T.H. Hodgson, Trailing edge noise prediction from measured surface pressures, *Journal of Sound and Vibration* 78 (1) (1981) 69–117.
[11] M.S. Howe, *Acoustics of Fluid-structure Interaction*, Cambridge University Press, Cambridge, UK, 1998.
[12] D.M. Chase, Modeling the wavevector-frequency spectrum of turbulent boundary layer wall pressure, *Journal of Sound and Vibration* 70 (1) (1980) 29–67.
[13] G.M. Corcos, Resolution of pressure in turbulence, *Journal of the Acoustical Society of America* 35 (1963) 192–199.
[14] T.F. Brooks, D.S. Pope, M.A. Marcolini, Airfoil self-noise and prediction, *NASA Reference Publication* 1218 (1989).
[15] R.K. Amiet, Effect of the incident surface pressure field on noise due to turbulence flow past a trailing edge, *Journal of Sound and Vibration* 47 (3) (1978) 387–393.
[16] M. Roger, S. Moreau, Trailing Edge Noise Measurements and Prediction for Subsonic Loaded Fan Blades, *AIAA paper* 2002-2460 (2002).
[17] M. Roger, S. Moreau, Back-scattering correction and further extensions of Amiet's trailing-edge noise model, Part 1: Theory, *Journal of Sound and Vibration* 286 (2005) 477–506.
[18] R.K. Amiet, Acoustic radiation from an airfoil in a turbulent stream, *Journal of Sound and Vibration* 41 (4) (1975) 407–420.